

# Perovskite Solar Cells with Carbon-Based Electrodes – Quantification of Losses and Strategies to Overcome Them

Dmitry Bogachuk, Bowen Yang, Jiajia Suo, David Martineau, Anand Verma, Stephanie Narbey, Miguel Anaya, Kyle Frohna, Tiarnan Doherty, David Müller, Jan P. Herterich, Salma Zouhair, Anders Hagfeldt, Samuel D. Stranks, Uli Würfel, Andreas Hinsch,\* and Lukas Wagner

Carbon-based electrodes represent a promising approach to improve stability and up-scalability of perovskite photovoltaics. The temperature at which these contacts are processed defines the absorber grain size of the perovskite solar cell: in cells with low-temperature carbon-based electrodes (L-CPSCs), layer-by-layer deposition is possible, allowing perovskite crystals to be large (>100 nm), while in cells with high-temperature carbon-based contacts (H-CPSCs), crystals are constrained to 10–20 nm in size. To enhance the power conversion efficiency of these devices, the main loss mechanisms are identified for both systems. Measurements of charge carrier lifetime, quasi-Fermi level splitting (QFLS) and light-intensity-dependent behavior, supported by numerical simulations, clearly demonstrate that H-CPSCs strongly suffer from non-radiative losses in the perovskite absorber, primarily due to numerous grain boundaries. In contrast, large crystals of L-CPSCs provide a long carrier lifetime (1.8  $\mu\text{s}$ ) and exceptionally high QFLS of 1.21 eV for an absorber bandgap of 1.6 eV. These favorable characteristics explain the remarkable open-circuit voltage of over 1.1 V in hole-selective layer-free L-CPSCs. However, the low photon absorption and poor charge transport in these cells limit their potential. Finally, effective strategies are provided to reduce non-radiative losses in H-CPSCs, transport losses in L-CPSCs, and to improve photon management in both cell types.

## 1. Introduction


Following remarkably rapid development of power conversion efficiencies (PCEs) of perovskite solar cells (PSCs) in the past years,<sup>[1,2]</sup> the stability of perovskite-based photovoltaic (PV) devices became the center of attention for numerous researchers across the globe.<sup>[3,4]</sup> While, numerous various techniques to solve this issue (e.g., passivation,<sup>[5,6]</sup> additive engineering,<sup>[7,8]</sup> barrier layer<sup>[9,10]</sup>) have been proposed so far, the most stable PSCs were achieved by the incorporation of a carbon-based back-contact.<sup>[11–13]</sup> Its highly hydrophobic properties, chemical inertness, and large thickness provide a strong protection of the sensitive layers underneath it from the ambient environment.<sup>[14]</sup> However, PCEs of PSCs with such carbon-based electrodes (CPSCs) are still behind the ones demonstrated in “conventional” PSCs with metal-based contacts, which is partially attributed to the lower conductivity of the graphite-based material, its contact to

D. Bogachuk, D. Müller, J. P. Herterich, S. Zouhair, U. Würfel, A. Hinsch, L. Wagner

Fraunhofer Institute for Solar Energy Systems ISE  
Heidenhofstr. 2, 79110 Freiburg, Germany  
E-mail: andreas.hinsch@ise.fraunhofer.de

B. Yang, J. Suo, A. Hagfeldt  
Laboratory of Photomolecular Science  
Institute of Chemical Sciences and Engineering  
École Polytechnique Fédérale de Lausanne (EPFL)  
Lausanne CH-1015, Switzerland

B. Yang, J. Suo, A. Hagfeldt  
Department of Chemistry  
Ångström Laboratory  
Uppsala University  
Uppsala SE-75120, Sweden

 The ORCID identification number(s) for the author(s) of this article can be found under <https://doi.org/10.1002/aenm.202103128>.

© 2022 The Authors. Advanced Energy Materials published by Wiley-VCH GmbH. This is an open access article under the terms of the Creative Commons Attribution License, which permits use, distribution and reproduction in any medium, provided the original work is properly cited.

DOI: 10.1002/aenm.202103128

D. Martineau, A. Verma, S. Narbey  
Solaronix SA

Rue de l'Ouriette 129, Aubonne 1170, Switzerland

M. Anaya, K. Frohna, T. Doherty, S. D. Stranks

Cavendish Laboratory  
Department of Physics  
University of Cambridge  
JJ Thomson Avenue, Cambridge CB3 0HE, UK

M. Anaya, S. D. Stranks  
Department of Chemical Engineering & Biotechnology  
University of Cambridge  
Philippa Fawcett Drive, Cambridge CB3 0AS, UK

D. Müller, J. P. Herterich, U. Würfel  
Materials Research Center FMF  
University of Freiburg  
Stefan-Meier-Str. 21, 79104 Freiburg, Germany

S. Zouhair  
Abdelmalek Essaadi University  
FSTT  
Thin Films & Nanomaterials Lab  
Tangier 90000, Morocco

the layer underneath, higher parasitic absorption coupled with rather poor reflection and not well-aligned electrode work-function.<sup>[14]</sup>

In 2013, Ku et al. have been the first to propose the concept of a CPSC, where the carbon-based contact would need a high-temperature treatment (400 °C) for removal of organic solvents and binders.<sup>[15]</sup> As hybrid lead-halide perovskites degrade at temperatures above 150 °C,<sup>[16]</sup> this implies that the perovskite cannot be introduced into the cell stack before this electrode is deposited. Therefore, each layer of the device stack needs to be mesoporous to allow the perovskite to be added at the last processing step. These PSCs with a carbon-based electrode cured at high temperatures (H-CPSCs) are particularly attractive for perovskite PV commercialization, since the entire cell stack can be deposited on a large scale using industrially relevant manufacturing techniques.<sup>[17–19]</sup> Recently we have shown that utilization of perovskite solar modules with such carbon-based electrodes can effectively reduce the CO<sub>2</sub>-footprint of the PV module down to 3.35 g CO<sub>2</sub>-eq./kWh, which is less than 5% of the CO<sub>2</sub>-footprint of the conventional silicon-based module.<sup>[17]</sup> Such a strong reduction of the green-house emissions during PV module manufacturing would be tremendously helpful in reducing the negative anthropogenic impact on the environment, especially if we aim towards terawatt-scale PV systems in the near future.

Shortly after the development of H-CPSCs, an alternative approach was proposed, based on the development of a carbon paste which contains solvents and binders that can be removed at lower temperatures allowing for the electrode deposition after the perovskite is introduced.<sup>[20,21]</sup> These PSCs with a low-temperature cured carbon-based contact (L-CPSCs) have several advantages regarding the degrees of freedom during device preparation (e.g., layer-by-layer deposition, wide range of applicable charge transport layers, compatibility with flexible substrates).<sup>[14]</sup> For comparison, the current PCE record of L-CPSCs is >20%,<sup>[22]</sup> which is still slightly above the recently obtained record of 18.1% PCE in H-CPSCs (whereby it is noteworthy that the latter did not have a hole-selective layer).<sup>[23]</sup>

Although CPSCs become more and more attractive in terms of stability, up-scalability, and low CO<sub>2</sub>-footprint,<sup>[14,17]</sup> so far, a quantitative comparison between the H-CPSCs and L-CPSCs has not been reported. Identifying why cell properties differ and ideally combining the advantages of both types is of paramount importance for developing highly efficient and stable perovskite PV devices with carbon-based electrodes. Here, we scrutinize the fundamental differences between these two types of CPSCs, starting from analyzing the key difference in the perovskite layer, namely the number of grain boundaries in the photoabsorber. First, we use numerical simulations to study the influence of the number of grain boundaries on CPSC performance losses, which shows that the quasi-Fermi level splitting (QFLS) is reduced in cells with smaller grains. This agrees with our experimental evidence demonstrating that even for an identical perovskite composition the QFLS is indeed lower in H-CPSCs than in L-CPSCs. Moreover, the charge carrier lifetime in perovskite with large grains (as utilized in L-CPSCs) is higher by over one order of magnitude than in perovskite with smaller grains (similarly to H-CPSCs) suggesting a lower non-radiative recombination rate and resulting in a strong

difference of almost 120 mV in the final open-circuit voltage ( $V_{OC}$ ) of these devices. Furthermore, we analyze the origins of the fill factor (FF) losses, constituted by non-radiative recombination and transport losses. Disentangling between different individual contributions to the transport losses we are able to identify promising methods to improve carrier extraction and transport. Finally, we combine all the presented evidence to outline a roadmap for the most promising routes to achieve high PCEs in CPSCs. This work paves the way for scientists in the perovskite community to accelerate the development of advanced, efficient, stable, low-cost, and sustainable perovskite PV devices with carbon-based electrodes, which contain enormous potential for industrialization and bringing humanity closer towards climate change goals.

## 2. Results and Discussion

### 2.1. Two Types of Perovskite Solar Cells with Carbon-Based contacts (CPSCs)

Although H-CPSCs and L-CPSCs both belong to the group of PSCs with carbon-based electrodes, they display significant differences in the device architecture and their opto-electronic characteristics. L-CPSCs are made using layer-by-layer deposition, allowing us to precisely control the perovskite layer thickness and grain size, whereas the H-CPSCs are manufactured by the deposition of all the mesoporous layers first, which are later infiltrated by the perovskite solution. Since the pore size in the mesoporous titanium oxide (m-TiO<sub>2</sub>) and zirconium oxide (ZrO<sub>2</sub>) layers of H-CPSCs are typically in the range of 10–20 nm, the perovskite crystals are most probably constrained to this size (Figure 1a), inducing numerous grain boundaries (GBs) along the entire solar cell stack, presumably causing non-radiative recombination and hindering carrier transport. In contrast, in L-CPSCs the perovskite crystals can reach sizes of hundreds of nanometers, (potentially) providing a single grain along the entire layer thickness, which is likely to be beneficial for the solar cell performance (Figure 1b). Thus, one of the most fundamental differences in the absorber layer between both cell types is the number of GBs and the transport distance.

### 2.2. Numerical Simulation of Neat Perovskite and CPSCs with Different Grain Boundary Densities

In order to evaluate the effect of GBs on the solar cell performance, we first simulate perovskite layer and CPSCs according to the standard representation of GB in silicon-based material, where creation of vacancies as well as bent, strained, or broken bonds is typically observed, all of which increases the defect density at the GBs in case the defects are not passivated.<sup>[24–26]</sup> In this case, the charge carriers trapped at these defects build up a charge  $Q_{GB}$ , which is compensated by accumulating the opposite type of free charge carriers from the bulk at the GB due to Coulombic forces.<sup>[27]</sup> This leads to the creation of a space-charge region (SCR) and hence an electric field at the GB, bending the energy bands, similarly to semiconductor-metal-semiconductor contacts (Figure 1c).<sup>[24]</sup>

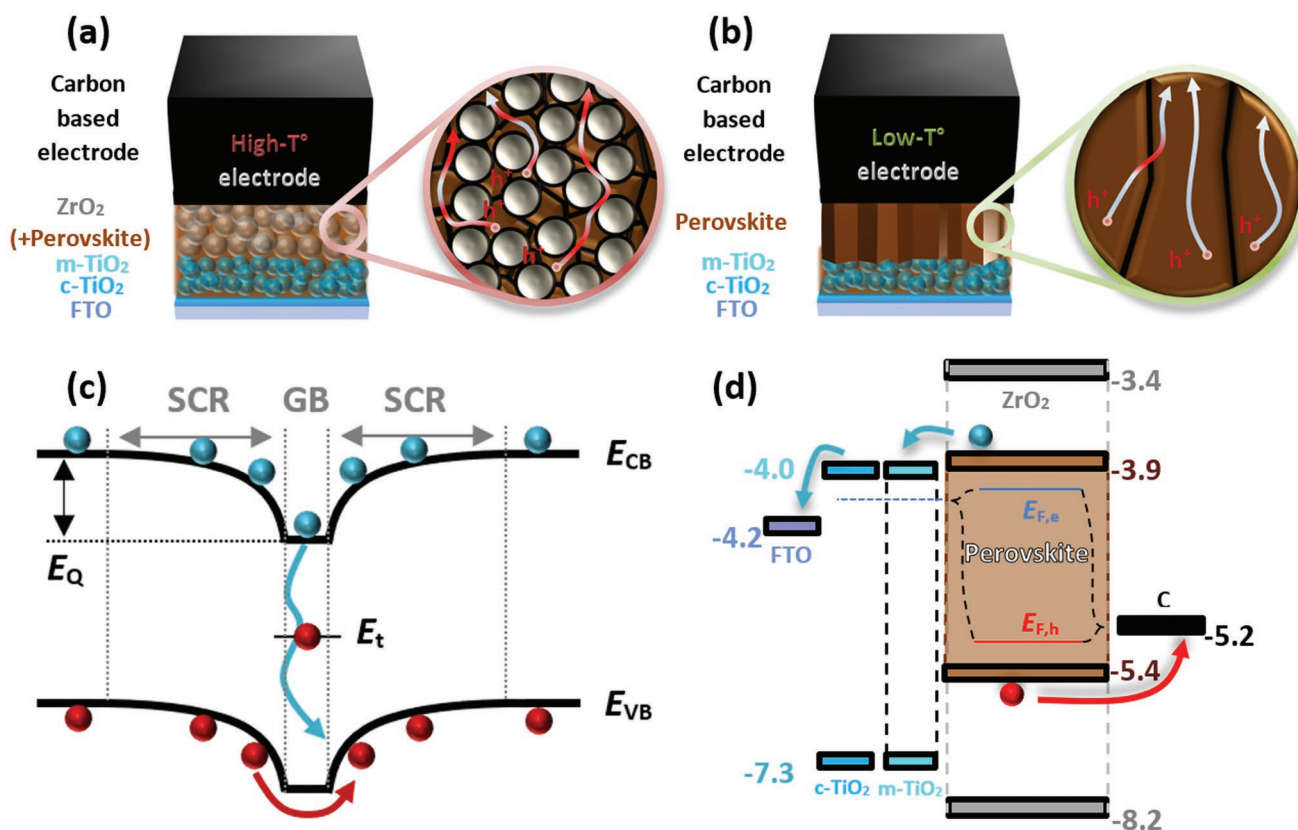


**Figure 1.** a,b) Illustration of two types of perovskite solar cells with carbon-based back-electrodes (CPSCs), showing cell stacks and charge carrier transport, which in the case of CPSCs with electrodes treated at high-temperature (H-CPSCs) is hindered by multiple grain boundaries in the perovskite layer due to constrained pore size of the  $ZrO_2$  layer. c) Energy band diagram of the region with charged grain boundary (GB) having a band offset of  $E_Q$ , inducing a space-charge region (SCR) which extends toward the bulk of the grains, providing non-radiative recombination pathways and hindering the transport of holes, by creating a potential barrier. d) Energy band diagram of CPSCs, where the electrons (blue) are extracted by  $m-TiO_2$  and further conducted to the front electrode, whereas holes (red) are extracted by carbon-based back-electrode.

According to several reports investigating the nature of grain boundaries in perovskites, the band bending at GBs in perovskite is normally downwards,<sup>[27,28]</sup> likely to be due to charged iodide vacancies ( $V_I^+$ ), implying positively charged GBs.<sup>[26]</sup> Consequently, on one hand the holes have to overcome a potential barrier at the GB, perturbing the carrier flow and negatively affecting the mobility and overall resistivity, while on the other hand, more electrons will recombine non-radiatively via the defect energy level  $E_t$ . Although in this work we implement the aforementioned GB representation in our simulation, we also note that different processing conditions can significantly affect structural properties of GB in perovskite films, even though its composition is the same.<sup>[29]</sup> Hence, the GB simulation in different halide perovskite films or layers has to be carried with great caution, as there is no generalized model developed at the moment, according to our knowledge.<sup>[30]</sup>

We first evaluate the impact of the GBs on the QFLS in neat perovskite absorber (400 nm thick) by using a SCAPS numerical simulation tool, utilizing drift-diffusion model (simulation parameters are described in Table S1, Supporting Information). Although it is a 1D model (meaning that it does not allow for lateral variations in properties) the vertical grain stacking is more detrimental for the carrier transport, which could be

simulated in SCAPS. Each grain boundary was simulated based on the energetic band diagram in Figure 1c which transverses across the perovskite layer thickness. Here only one type of GB was considered with properties (e.g.,  $E_t$ ,  $Q_{GB}$ ) adjusted to match the experimental values determined in literature for a similar type of perovskite.<sup>[31,32]</sup> Figure 2a depicts how the high number of grain boundaries (i.e., smaller grain size) lowers the QFLS of the perovskite photoabsorber. In this model, a crystalline  $MAPbI_3$  ( $MA - CH_3NH_3^+$ ) absorber layer with an (ideal) single grain along the layer thickness has a QFLS of 1.33 eV (which is the radiative limit for perovskite absorber with energy bandgap of 1.6 eV<sup>[33–35]</sup>). Introducing one GB along the layer thickness (leading to the grain size of 200 nm) with a trap density  $N_t = 10^{16} \text{ cm}^{-3}$  (Figure 2a) reduces the splitting already by 100 meV. For comparison, several reports have demonstrated that the typical defect densities in perovskite films (most of which are shallow traps) are in the range of  $10^{17}–10^{19} \text{ cm}^{-3}$ ,<sup>[31,36,37]</sup> with deep trap densities in the order of  $10^{15}–10^{16} \text{ cm}^{-3}$ , which dominate the non-radiative recombination.<sup>[38]</sup> Notably, even if one considers a very optimistic case of non-radiative recombination exclusively at the GBs with a very low  $N_t = 10^{14} \text{ cm}^{-3}$ , a PSC with a grain size of 25 nm, which is similar to the crystal size found in H-CPSCs,<sup>[39]</sup> would still have a reduction of QFLS by  $\approx 63 \text{ meV}$ .

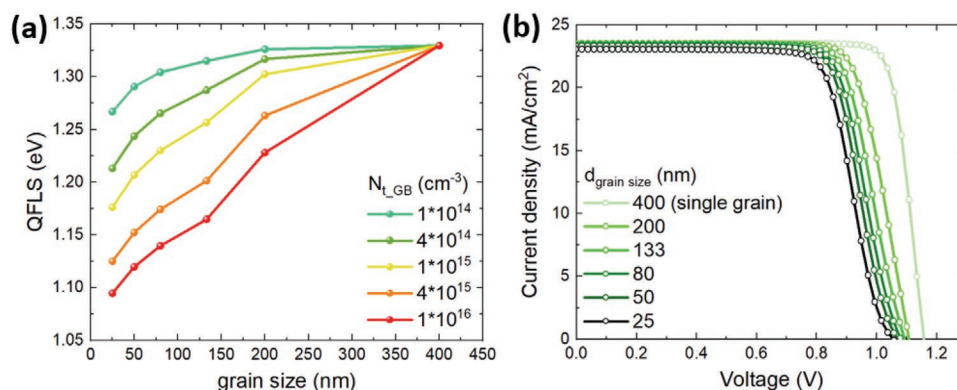


**Figure 2.** a) QFLS in simulated neat perovskite films with different numbers of grain boundaries. b)  $J$ - $V$  curves of the simulated CPSCs with different numbers of grain boundaries. The cell parameters can be found in Figure 1d and Table S1, Supporting Information.

To further demonstrate the negative effect of GBs on the final solar cell performance, we simulate the hole-transport-layer (HTL)-free PSC with a carbon-based back-contact, according to the energy band diagram shown in Figure 1d (more detailed simulation parameters can be found in Table S2, Supporting Information). In order to focus only on the contribution of grain boundaries on the performance loss, in this simulation we only consider non-radiative recombination at the GBs and ignore interfacial recombination at charge extraction layers. In Figure 2b the  $J$ - $V$  curves of the simulated cells are depicted where the FF and the  $V_{OC}$  are significantly affected by grain-boundaries, whereas the short-circuit current density ( $J_{SC}$ ) is affected only slightly.

The non-radiative recombination can affect not only the QFLS, and consequently the  $V_{OC}$ , but also the FF, especially with a considerable amount of recombination happening at the interfaces.<sup>[40]</sup> In order to demonstrate the effect of GBs on non-radiative recombination we first look at the  $V_{OC}$ , which in the case of radiative limit can be defined as:<sup>[33,41]</sup>

$$V_{oc,rad} = \frac{k_B T}{q} \ln \left( \frac{J_G}{J_{0,rad}} + 1 \right) \quad (1)$$

where  $k_B$  is Boltzmann constant,  $T$  is temperature,  $q$  - elementary charge,  $J_G$  - photogeneration current, and  $J_{0,rad}$  - radiative thermal equilibrium recombination current density in the dark (which in the absence of non-radiative recombination is equal to the dark saturation current  $J_0$ ).  $J_G$  and  $J_{0,rad}$  can be found by multiplying  $q$  with an integrated product of external quantum efficiency ( $EQE_{PV}$ ) and incident photon flux, namely of AM1.5G for  $J_G$  and of black body ( $T_{BB} = 300\text{K}$ ) for  $J_{0,rad}$ , respectively (detailed derivation is shown in Note S1, Supporting Information).

The  $EQE_{PV}$  onset and the emitted photon flux in the dark  $\Phi_{em}$  of the simulated CPSCs with different grain sizes are presented in Figure S1, Supporting Information. As one can see, the  $EQE_{PV}$  is affected by the grain size especially in the region close to the bandgap energy, reducing both:  $J_{0,rad}$  and  $J_G$ . The calculated values are presented in Table S3, Supporting Information. Based on the difference between the obtained  $V_{OC,rad}$  and the final  $V_{OC}$  of the simulated CPSCs we can estimate the  $V_{OC,loss}$

that is lost due to the contribution of non-radiative recombination, which increases with the higher number of grain boundaries (Table S3, Supporting Information).

The calculated external photoluminescence quantum yield (PLQY) is shown in Table S3, Supporting Information, which is the lowest for samples with most GBs along the cell thickness and is the highest in the CPSCs without any GBs, where the photoluminescence quantum yield (PLQY) approaches 2.5%. Moreover, the total dark saturation current  $J_0$  is lowest in simulated CPSCs without GBs and is the highest in cells with a perovskite grain size of 25 nm, due to large contribution of recombination-active traps at the GBs. The simulation results demonstrate, that reducing the grain-boundaries in CPSCs should significantly help to reduce non-radiative recombination in the cell, slightly improve the light-absorption near the band edge and thus boost its  $V_{OC}$  (as the higher  $V_{OC}$  is a consequence of reduced non-radiative recombination) and overall PCE. Now we move from the numerical simulation of CPSCs with GBs to the actual manufactured devices.

## 2.3. Properties of Perovskite Layer in CPSCs

### 2.3.1. Morphological and Crystallographic Differences

In order to compare non-radiative losses of perovskite layers in both L-CPSCs and H-CPSCs, we first analyze the properties of a pristine absorber layer. For this, the perovskite has to be deposited on a dielectric substrate that does not allow for charge carrier extraction, such as glass. The  $\text{ZrO}_2$  layer, in which the absorber layer in H-CPSCs is normally embedded into, is also dielectric as it has a conduction band minimum at around  $-3.4$  eV and a valence band maximum at around  $-8.2$  eV (Figure 1b),<sup>[42,43]</sup> meaning that it can neither extract electrons nor holes from the perovskite. Therefore, to mimic the perovskite absorber behavior in H-CPSCs, we deposited perovskite in a  $\text{ZrO}_2$  porous layer (of same thickness as in complete solar cells) on glass substrates. To ensure that perovskite completely fills the pores of a  $\text{ZrO}_2$  layer without having any capping layer on top, here we employ ink-jet pipetting to precisely control the filling conditions, producing samples that we further refer to as perovskite in porous layer (PiPL). The perovskite as planar layer (PaPL) was spin-coated

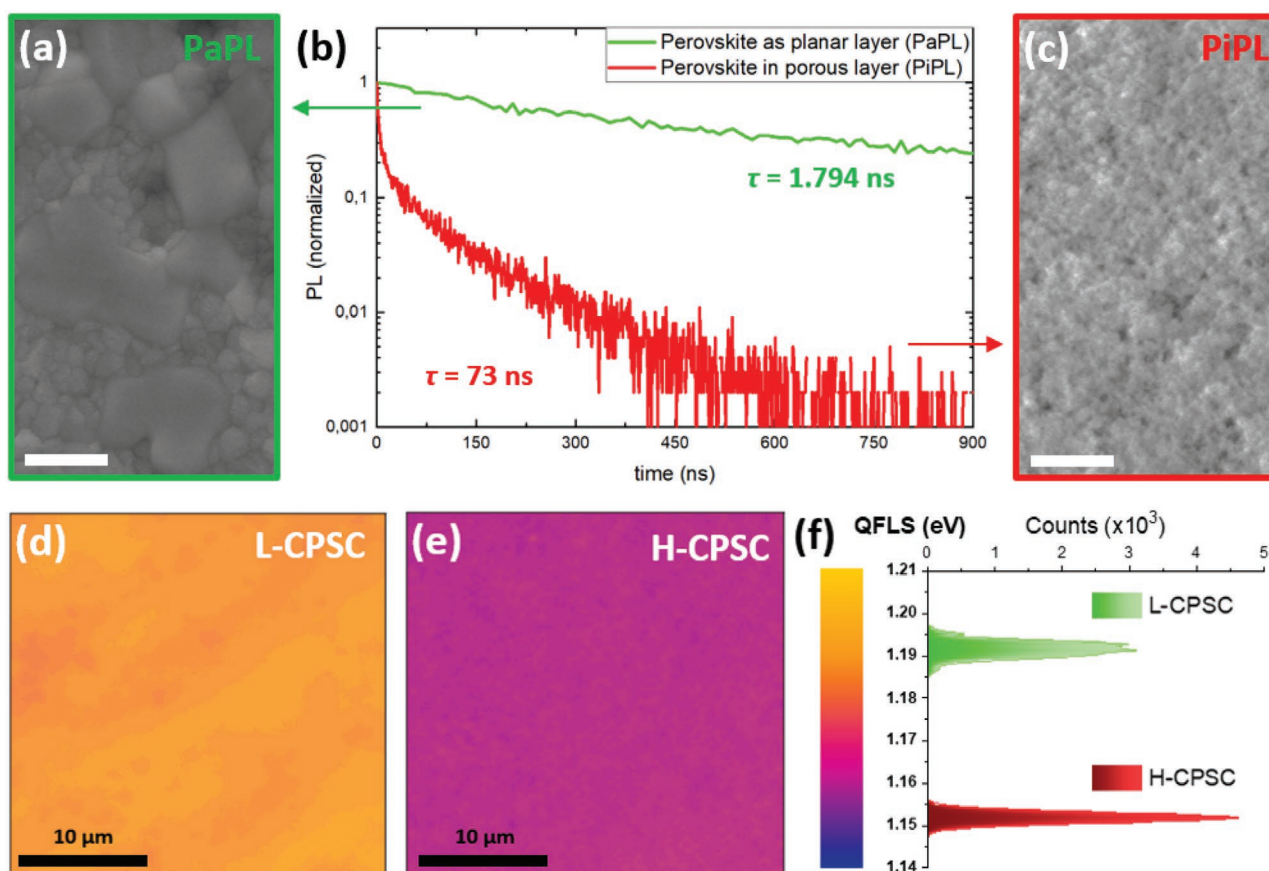
on glass to produce a 350 nm film which is normally used to manufacture complete L-CPSCs. For the entire study, we utilize  $5\text{AVA}_{1-x}\text{MA}_x\text{PbI}_3$  perovskite (5AVA-aminovaleric acid, MA-methylammonium and  $0 < x < 1$ ), which has been a popular choice of perovskite in H-CPSCs over the last years, due to high moisture retention properties, favorable anchoring of the carboxylic acid group to the  $\text{TiO}_2$  during crystallization, and improved infiltration through the porous scaffold.<sup>[42,44,45]</sup>

Figure S2a, Supporting Information shows the cross-sectional view of the PiPL displaying the absence of any capping layer above  $\text{ZrO}_2$ , while simultaneously filling the porous layer homogeneously across its entire thickness. Looking at the AFM images (Figure S3, Supporting Information) of both layers we note that the PaPL has a smooth surface morphology with a 12.9 nm average surface roughness in comparison to a larger value of 19.5 nm in the case of PiPL. The X-ray diffraction measurements in Figure S4, Supporting Information, show much more pronounced peaks corresponding mostly to  $\text{MAPbI}_3$  (since the amount of 2D  $5\text{AVAPbI}_4$  perovskite is rather small) perovskite in PaPL than in PiPL due to higher degree of crystallinity. However, the diffraction angle of core reflection planes (e.g., (110) and (220)) remains the same in PaPL and PiPL, confirming that the perovskite crystal structure and lattice dimensions are nearly identical in both configurations, planar and mesoscopic.

### 2.3.2. Non-Radiative Losses in Perovskite Absorber due to Grain Boundaries

To quantify the charge carrier lifetime in PiPL and PaPL we first carried out time-resolved photoluminescence (TRPL) measurements (Figure 3b). From the transient photoluminescence response in the high-level injection regime the lifetime for PiPL was found to be much lower than that of the PaPL: 72.9 ns in comparison to that of nearly 1.8  $\mu\text{s}$  in planar films. This astonishing difference in carrier lifetime, despite identical perovskite (elemental) composition, demonstrates the presence of excessive non-radiative recombination in PiPL, most likely due to numerous GBs as discussed earlier. This will have detrimental effects on the  $I$ - $V$  parameters of the H-CPSCs, especially  $V_{\text{OC}}$ . Although  $V_{\text{OC}}$  is not affected by diffusion length (which is coupled to carrier lifetime by definition) in first order, it is strongly influenced by the lifetime and therefore the potential of H-CPSCs to reach high PCEs becomes limited.

Although it has been often demonstrated that grain-size engineering in perovskite films is a promising method to reduce the non-radiative recombination at GBs,<sup>[31,46-49]</sup> more studies suggest that the exact nature of GBs and their effect on PSC performance is still ambiguous.<sup>[27]</sup> The intuitive affiliation of GBs with differences in morphological properties of



**Figure 3.** Top-view SEM image of a) perovskite as planar layer (PaPL) and c) perovskite in porous layer (PiPL). b) Time-resolved photoluminescence (TRPL) measurement of perovskite produced as a planar layer (as it is done in L-CPSCs) and perovskite embedded in nanoporous  $\text{ZrO}_2$  (as it is done in H-CPSCs). Scale bar – 300 nm. QFLS maps of d) PSC with a low-temperature cured carbon electrode (L-CPSC) and e) with high-temperature cured carbon-electrodes (H-CPSC). f) The color scale and pixel distributions for each sample.

perovskite films (as can be seen from, for example, scanning electron microscopy SEM images) does not account for sub-grain crystallographic heterogeneity within the same morphological domain.<sup>[50–52]</sup> highlighting that for the exact identification of a GB in halide perovskite, diffraction-based techniques are required.<sup>[30,53]</sup> In this work, however, we use the term grain boundary to describe “morphological grains boundaries”, observed from SEM measurements. Although, these morphological grain boundaries do not define the dimensions of a continuous uninterrupted perovskite lattice, an experimental evidence shown in literature suggests that larger morphological grains visible from SEM also result in larger grains with the same orientation.<sup>[52]</sup> The top-view SEM images (Figure 3a,c) confirm that PaPL indeed includes large-sized perovskite crystals (with some small crystals in between as well).

Next, we utilize hyperspectral absolute PL imaging on PiPL and PaPL to evaluate the local non-radiative recombination of neat perovskite layers (Figure S5a,b, Supporting Information) and complete cells in both configurations: L-CPSCs and H-CPSCs (Figure S7, Supporting Information). The obtained PL maps, clearly demonstrate that samples with large perovskite crystals (PaPL and L-CPSC) exhibit higher photoluminescence intensity, highlighting the reduced non-radiative recombination in these samples, and suggesting a lower number of defects. Notably, we observe a slight difference in the PL peak position, where the samples with larger crystals are red-shifted by  $\approx 3$  nm, relative to the spectral peak position of the sample with small crystals (Figure S7c, Supporting Information). We attribute this to a change in Pb–I bond strain and its effect on the material bandgap, when perovskite grains differ in size, as was demonstrated in earlier works.<sup>[54–58]</sup>

To confirm our hypothesis that the perovskite/ZrO<sub>2</sub> interface does not introduce an additional loss channel for non-radiative recombination, we carried out absolute photoluminescence measurements (detecting all photons, arising from the radiative recombination in the semiconductor) on PaPL samples deposited on top of glass, ZrO<sub>2</sub>, and m-TiO<sub>2</sub> (Figure S6, Supporting Information). The PL intensity is similar in samples deposited on glass and ZrO<sub>2</sub>, suggesting that ZrO<sub>2</sub> does not cause a reduction in PL (and therefore charge-carrier densities). For comparison, m-TiO<sub>2</sub>/PaPL sample has a significantly reduced PL intensity due to additional quenching of charge-carriers. Thus, we confirm that the perovskite/ZrO<sub>2</sub> interface does not introduce a noticeable non-radiative recombination mechanism and the reduction in PL, QFLS, and carrier lifetime in H-CPSCs is ascribed to numerous grain boundaries of perovskite embedded into the nano-porous ZrO<sub>2</sub> and not to perovskite/ZrO<sub>2</sub> interface.

Such absolute steady-state PL measurement also allows for precise quantification methods to experimentally determine the QFLS in solar cells.<sup>[59,60]</sup> Assuming that for the photons with energies higher than the PL maximum, the material absorptivity approaches unity, Würfel’s generalized Planck law can be used to extract the QFLS from the high-energy slope of the PL spectrum (more details in Note S4, Supporting Information).<sup>[61,62]</sup> Using the PL maps in Figures S5a and S5b, Supporting Information, we construct the QFLS maps of L-CPSCs and H-CPSCs shown in Figures S5d and S5e, Supporting Information.

It was already demonstrated in the photovoltaic community that the QFLS in PSCs is strongly reduced by the interfaces between absorber and a charge-selective layer.<sup>[40,61,63]</sup> By comparing the QFLS of the neat perovskite with large crystals (PaPL) shown in Figure S5d, Supporting Information, with the QFLS of L-CPSC shown in Figure 3d, one can observe that the introduction of charge selective layers reduces the QFLS by less than 20 meV, highlighting that the interfacial non-radiative recombination in this cell type is not only low, but comparable (or in some cases even better) with the state-of-the-art p-i-n and n-i-p stacks.<sup>[40,63]</sup> In contrast, the QFLS of the H-CPSC is reduced by 40 meV to 1.15 eV. We note that the difference in QFLS of the H-CPSCs and L-CPSCs correlates with the commonly observed large difference in  $V_{OC}$  between the H-CPSCs and the L-CPSCs (a comparison of the reported  $V_{OC}$ s for H- and L-CPSCs can be found in Figure S8, Supporting Information).

## 2.4. Analysis of Manufactured CPSCs with Low- And High-Temperature Carbon-Based Electrodes

### 2.4.1. Non-Radiative Losses in CPSCs

Next, we manufactured H- and L-CPSCs using the same charge-transport layers and the same perovskite composition, to focus only on the absorber layer and to scrutinize an objective comparison between these two structures. We note that the optimal layer thicknesses for each structure are different, and in order to compare only the effect of the absorber layer on the device performance, all the layers in the stack have been optimized to reach the highest efficiency in both device configurations. Cross-sectional SEM images (Figure S9, Supporting Information) show that the m-TiO<sub>2</sub> layer had thicknesses of  $\approx 150$  and 500 nm in L-CPSCs and H-CPSCs, respectively. The perovskite layer in L-CPSCs had a thickness of  $\approx 350$  nm, while in the case of H-CPSC it is embedded into a 1  $\mu$ m thick ZrO<sub>2</sub> layer. Although L-CPSCs have a thinner layer thickness which implies a lesser charge carrier generation, as will be shown below, still the  $V_{OC}$  and QFLS are higher. This indicates lower non-radiative recombination and hence a higher number of photoexcited carriers. Both types of cells had an  $\approx 10$ –12  $\mu$ m thick carbon layer completing the cell stack.

The  $J$ – $V$  parameters of the manufactured devices with mesoscopic and planar configurations are shown in Figure 4a–d. The average  $V_{OC}$  of the H-CPSCs is  $\approx 920$  mV, while some of the L-CPSCs have a  $V_{OC}$  above 1.1 V, which agrees with our previously shown long carrier lifetime, high photoluminescence intensity, and high QFLS in neat perovskite films of the L-CPSCs. This enormous difference in  $V_{OC}$  between the samples despite the same perovskite absorber and contact layers, also suggests that the photoluminescence yield in L-CPSCs is higher than in H-CPSCs by almost three orders of magnitude ( $k_B T/q \ln(10^3) \approx 180$  mV) (assuming  $T = 300$  K). We note that according to our knowledge there has not been any report yet on an HTL-free CPSC with a  $V_{OC}$  above 1.1 V, utilizing a perovskite with such an energy bandgap of 1.6 eV (Figure S8, Supporting Information). In Figure S10, Supporting Information, we show the  $V_{OC}$  and carrier lifetimes reported in literature, highlighting that these properties of our L-CPSCs are

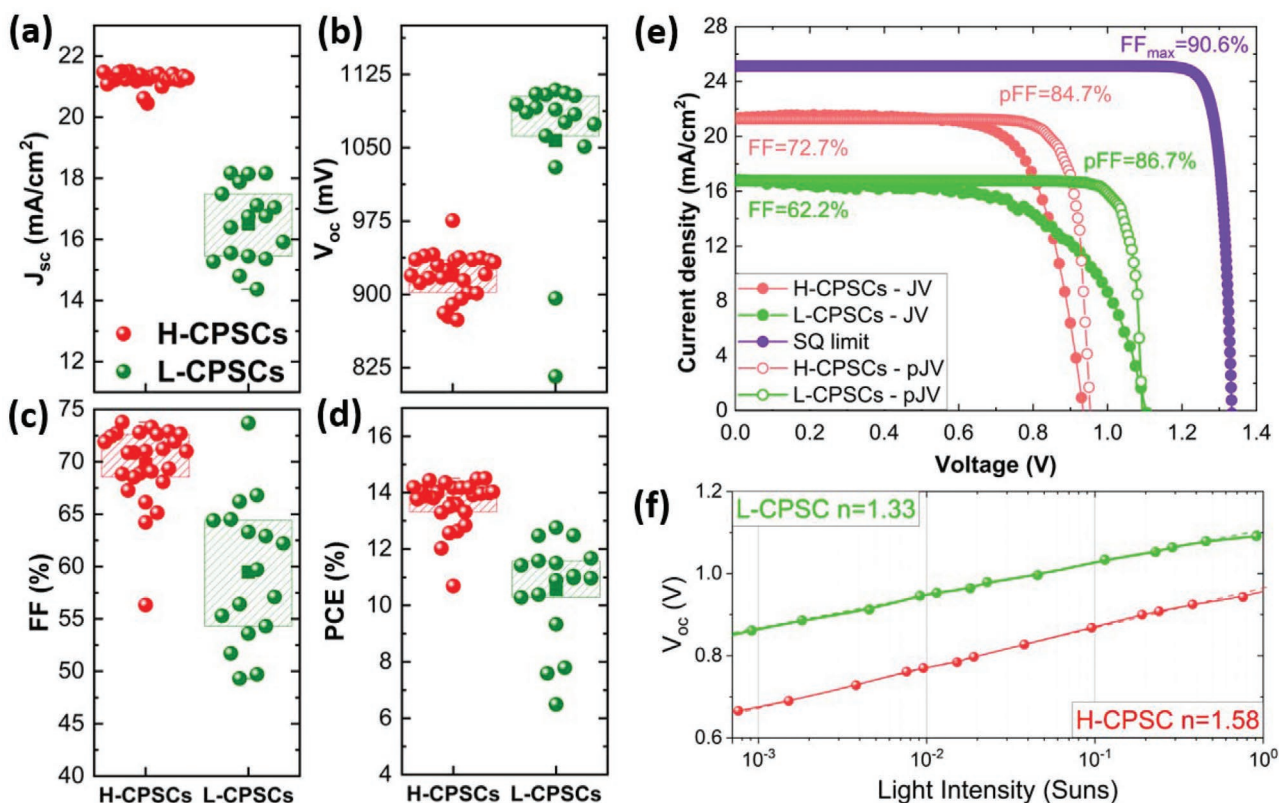


**Figure 4.** a–d) JV parameters of the manufactured H-CPSCs and L-CPSCs, e)  $J$ - $V$  curve of champion devices and pseudo- $J$ - $V$  curves obtained from  $V_{OC}$ -versus-light intensity measurement. Ideal  $J$ - $V$  curve of a solar cell with the utilized bandgap (purple), which is limited by radiative recombination (obtained from the Shockley–Queisser limit) is shown for comparison. f)  $V_{OC}$ -versus-light intensity measurement and the ideality factor  $n$  for L-CPSC.

comparable even with the state-of-the-art PSCs, containing an HTL and metallic electrode. Remarkably, the  $V_{OC}$  values of 1.1 V align well with the  $V_{OC}$  predicted by our simulations of CPSCs with a low number of grain boundaries (Table S3, Supporting Information). Namely CPSCs with only 1 or 2 grain boundaries along the absorber thickness have the  $V_{OC}$  close to 1.1 V, indicating the validity of our simulation.

Based on the obtained current densities  $J_G$  and  $J_{0,rad}$  (from  $EQE_{PV}$ ) we calculate  $V_{OC,rad}$  and  $V_{OC,loss}$ , which are presented in Table 1. Clearly, L-CPSCs exhibit lower  $V_{OC,loss}$  than the H-CPSCs due to lower non-radiative recombination at the grain-boundaries.

The structural disorder of the absorber causes an exponential tail in the absorption coefficient close to the absorption edge due to multiple sub-bandgap states. The slope of the exponential part, which depends on the degree of structural disorder is

**Table 1.** Opto-electronic parameters of manufactured H-CPSCs and L-CPSCs as determined by EQE,  $V_{OC}$ , and absolute PL measurements.

	H-CPSC	L-CPSC
$J_{0,rad}$ [ $\text{mA cm}^{-2}$ ]	$3.2 \times 10^{-21}$	$8.1 \times 10^{-22}$
$V_{OC,rad}$ [V]	1.302	1.33
$V_{OC,cell}$ [V]	0.913	1.109
$V_{OC,loss}$ [mV]	389	221
QFLS [eV]	1.15	1.192

also described by Urbach energy ( $E_U$ ).<sup>[41]</sup> Based on the  $EQE_{PV}$ , the Urbach energy for H-CPSCs and L-CPSCs was determined to be 25.8 and 18 meV (Figure S11, Supporting Information), respectively, which once again supports the hypothesis that the perovskite crystals grown inside mesoporous  $ZrO_2$  exhibit lower opto-electronic quality than in case of planar large crystals. In fact, Choi et al. have also demonstrated that in the mesoporous layers  $\approx 70\%$  of the embedded perovskite consist of a highly disordered phase which has significant consequences on the opto-electronic properties.<sup>[64]</sup>

Non-radiative recombination affects not only the  $V_{OC}$  losses but also the FF due to losses during carrier transport (including resistive losses at the GB interfaces). By measuring the dependency of  $V_{OC}$  on the incident light intensity, a so-called pseudo  $J$ - $V$  curve can be obtained, in order to disentangle between non-radiative and transport losses of the FF, where the latter are caused by resistance of the cell layers and interfaces between them.<sup>[40,65]</sup> Here we employ the same strategy to elucidate the effect of non-radiative and transport losses on the FF of CPSCs in both configurations. Figure 4e shows the ideal  $J$ - $V$  curve of a solar cell with the utilized bandgap, which is limited by radiative recombination (obtained from the Shockley–Queisser limit), as well as the obtained pseudo- $J$ - $V$  for the L-CPSCs and H-CPSCs. The pseudo-FF (pFF) were found to be 86.7% and 84.7% for the L-CPSC and H-CPSC, respectively. Clearly, the higher QFLS and lower non-radiative recombination in the perovskite absorber with larger crystals positively affects not only the  $V_{OC}$

as was shown earlier but also the FF, providing potential for such “planar” cells to reach higher efficiencies. Nevertheless, the actual FF of the L-CPSCs, obtained from the  $J$ - $V$  measurement is lower, suggesting that the transport losses play the dominant role in the reduction of the FF. We also note that the ideality factor  $n$ , describing the dominant recombination mechanism in the cell,<sup>[34]</sup> is rather low in MAPbI<sub>3</sub>-based L-CPSCs—only 1.33, in comparison to 1.58 in H-CPSCs (Figure 4f). This further supports our arguments that non-radiative recombination in L-CPSCs is reduced due to a lower number of GBs and carrier trap densities. However, the L-CPSCs seem to suffer more than H-CPSCs from the transport losses.

#### 2.4.2. Charge Extraction and Transport Losses in CPSCs

To look more in depth at the transport losses, we extract the series resistance ( $R_s$ ) of both cell types from the slope of the  $J$ - $V$  curve at  $V_{OC}$ . The  $R_s$  for H-CPSCs and L-CPSCs were determined to be 6.8 and 14.3  $\Omega\text{cm}^2$ , respectively. Based on the geometry of the cell and the transport distance for electrons and holes in the respective electrodes, the total electrode resistance was found to be similar in both cell types: 1.76  $\Omega\text{cm}^2$  for L-CPSCs and 1.25  $\Omega\text{cm}^2$  for H-CPSCs (a more detailed discussion of the electrode contribution to the total series resistance is provided in Note S5, Supporting Information).

Using electrochemical impedance spectroscopy (EIS), we were able to disentangle between the contribution of pure ohmic and charge transport losses. From Nyquist plots presented in Figure S12, Supporting Information, two semicircles appear, which correspond to the capacitor-like behavior of several interfaces of the stack. We attribute the high-frequency semi-circle to the charge transport resistance primarily at the carbon/perovskite interface,<sup>[66–69]</sup> from which a real part of the impedance can be extracted. In H-CPSCs the perovskite/carbon interface has an interfacial resistance of 3.04  $\Omega\text{cm}^2$ , whereas in L-CPSCs it was determined to be  $\approx 11.4 \Omega\text{cm}^2$  (obtained from fitting the Nyquist plot to the equivalent circuit in Figure S12, Supporting Information). This finding suggests that the interfacial resistance at the perovskite/carbon contact represents the main transport limitation of the L-CPSCs. To confirm this hypothesis, we needed to distinguish between the reduction of FF due to carbon electrode sheet resistance and perovskite/carbon interfacial resistance. Hence, to confirm this hypothesis, the carbon layer was removed from an H-CPSC device and a low-temperature carbon electrode was deposited instead. Thus, an L-CPSC electrode on an PiPL absorber layer has been produced. This allows us to compare the performance differences affiliated with the carbon electrode itself and the perovskite/carbon interface while the differences related to the perovskite absorber in both architectures need not be considered. From the  $J$ - $V$  curves before and after carbon electrode replacement in Figure S13, Supporting Information, we observe that the FF drops from nearly 70% to 58.8%, respectively, which agrees with the mean values of H-CPSCs and L-CPSCs (Figure 4c). We attribute this reduction in FF to a higher interfacial resistance at the perovskite/carbon interface. An effect of sheet resistances can be excluded, since the sheet resistance of a low-temperature carbon electrode is even lower than that of a high-temperature type.

During perovskite crystallization in the mesoscopic layers of H-CPSCs, pores provide multiple nucleation sites, leading to a rather heterogeneous nucleation and growth. Although such crystallization causes multiple defect-induced energy states in the neat perovskite (as demonstrated earlier), it also means that some crystals grow directly on the surface of the carbon-based electrode, which could explain the exceptionally low interfacial resistance of such cells demonstrated earlier. We also note that the second semicircle in the Nyquist plot, which is attributed to the recombination resistance (and therefore should be high) is 50 times larger in L-CPSCs than in H-CPSCs, supporting the previously shown non-radiative recombination analysis.

Another strong limitation of our L-CPSCs is the  $J_{SC}$ , which can be related to lower photon absorption, worse charge carrier extraction, or a combination of both. To compare the homogeneity of current extraction across the active area we measure the spatially resolved light-beam induced current (LBIC) under short-circuit condition. The light-beam induced current (LBIC) map in Figure 5a,b shows that the photogenerated current is produced homogeneously in the entire cell, although its value is higher in the H-CPSCs than in L-CPSC, which also correlates with the  $J$ - $V$  measurements.

In order to qualitatively resolve the differences in charge carrier extraction we perform spatially resolved PL measurements under open- and short-circuit conditions. The underlying principle of this novel characterization method is the following: under open-circuit the recombination rate is equal to the generation rate, hence, the excited charge carriers will recombine radiatively and non-radiatively, implying that in an ideal solar cell without non-radiative recombination the PL is homogeneous across the entire active area and as high as possible (limited by the maximum number of photoexcited carriers). However, under short-circuit the charge carriers are able to be extracted by the respective selective contacts and forwarded further to the external load, instead of recombining. Thus, it is favorable to see a low PL signal under a short-circuit condition and the difference between the PL of the cell under open- and short-circuit can be used as a qualitative measure to evaluate the charge extraction of the cell.<sup>[70]</sup> Figure 5c–f depicts that the PL of H-CPSC is almost one order of magnitude lower than that of L-CPSC (due to the excessive non-radiative recombination as was shown above). Switching from open circuit to short-circuit quenches the PL, suggesting that the charge extraction in both cell types is similar.

The external quantum efficiency (EQE) in Figure S14, Supporting Information, demonstrates that the L-CPSCs suffer from a lower light absorption, particularly in the long-wavelength region compared to H-CPSCs. The reduced absorption spectrum of PaPL in comparison to PiPL (due to lower layer thickness) was confirmed via UV-Vis reflectance and transmission spectra measurement in Figure S15, Supporting Information. This provides a plausible explanation why the  $J_{SC}$  values of L-CPSCs are lower than that of H-CPSCs.

## 2.5. Outlining Promising Strategies to Improve the PCE of CPSCs

We particularly highlight that the cell layers and perovskite composition were chosen to have as similar properties as possible,



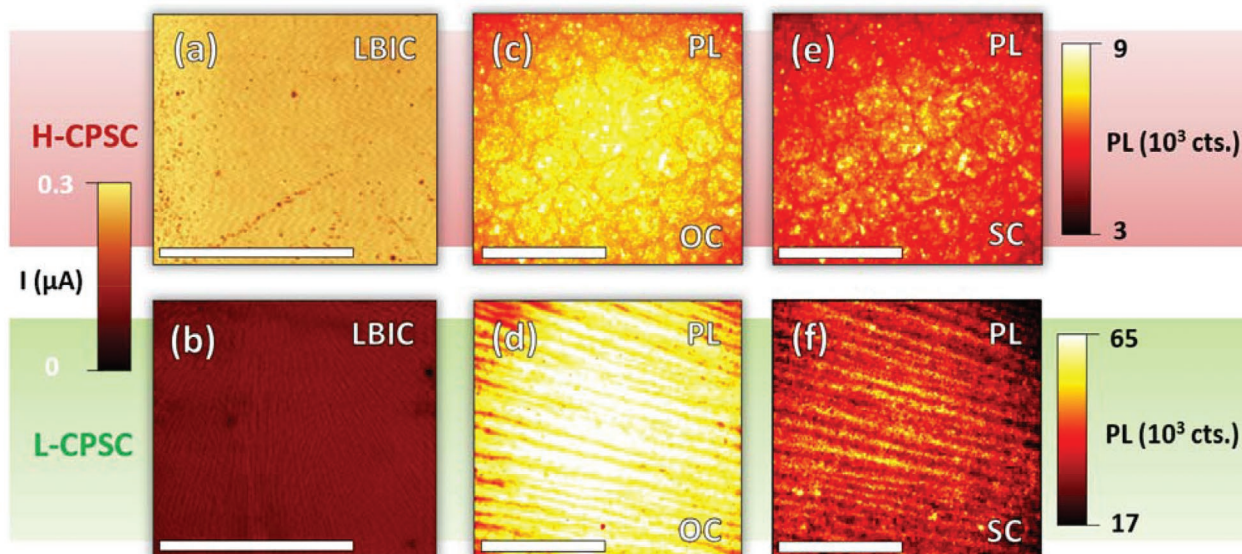


**Figure 5.** a,b) Light-beam induced current (LBIC) measurements of an H-CPSC and an L-CPSC. Scale bar – 4 mm. c–f) PL images of a H-CPSC and L-CPSC under open-circuit (c,d) and short-circuit (e,f), highlighting a difference in PL between these two states due to efficient charge extraction in both cell types. Scale bar – 0.4 mm. Note that the number of PL counts in L-CPSCs is higher than in H-CPSCs by almost one order of magnitude.

and to allow an objective comparison between the two types of stacks (rather than between two types of perovskite compositions or charge-extracting layers). Hence the conclusions drawn from this study can be applicable as well for the cases when other stacks are utilized.

Combining measurement results from the series resistance losses in both cell structures (Note S6, Supporting Information), it becomes clear that the FF in H-CPSCs is limited by the non-radiative losses, induced by numerous grain-boundaries, whereas the FF of L-CPSC strongly suffers from the interfacial resistance at the perovskite/carbon contact (Figure 6a). The losses in the electrodes can be reduced further by selecting a more conductive TCO front contact and the conductivity of the carbon-based contact can be improved by altering the graphite crystal type,<sup>[71]</sup> surface functionalization, and dopants.<sup>[14]</sup> Other ohmic FF losses, except for the electrodes are negligible, while

additional FF losses, could possibly be alleviated by improving perovskite/TiO<sub>2</sub> contact and reducing its interfacial resistance.

Figure 6b,c depicts the main free power losses in both cell structures, serving as a guideline for the main strategies to improve the PCE of both types of CPSCs:

- i. Non-radiative losses in H-CPSCs strongly limit the potential of such cells to reach higher efficiencies, especially the  $V_{OC}$ . To date, the highest photovoltages in H-CPSC with MAPbI<sub>3</sub> absorbers are only slightly above 1.0 V.<sup>[72]</sup> Considering that one of the key limitations of  $V_{OC}$  is due to numerous GBs, pore-size engineering seems to be a promising strategy to allow for the growth of large perovskite crystals in a “microporous” scaffold (as opposed to a nanoporous scaffold in H-CPSCs). Up to now, only few reports have focused on optimizing the pore size of mesoscopic layers to improve the photovoltaic performance of the PSCs<sup>[73,74]</sup> and this strategy needs to be

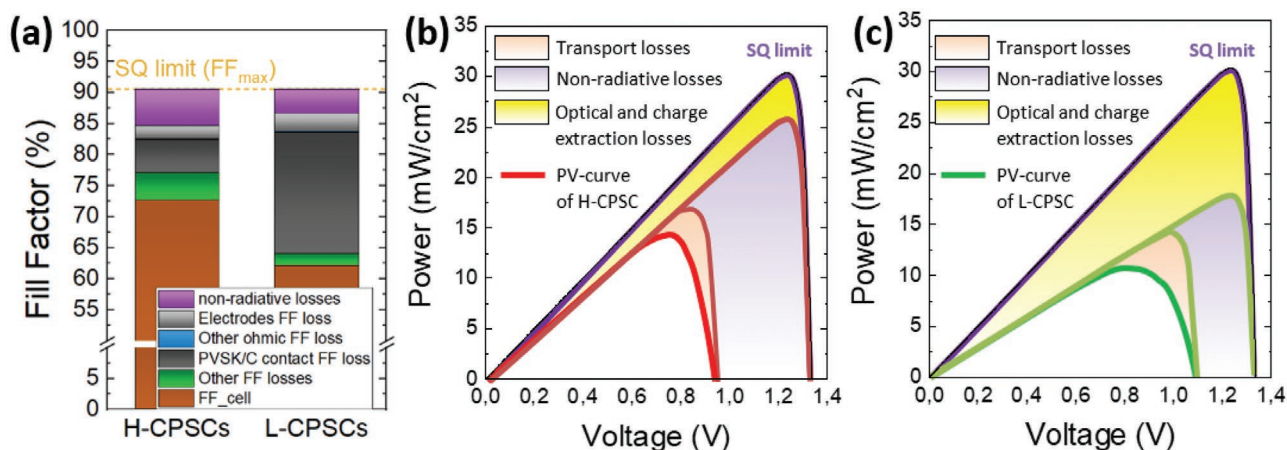


**Figure 6.** Results from the combinatory analysis of PSCs with carbon-based electrodes. a) Distribution of FF losses in H-CPSCs and L-CPSCs. Visualization of power density–voltage (PV) curves of b) H-CPSCs and c) L-CPSCs, illustrating the power losses and their origins

further explored. Naturally, methods to passivate the GBs and reduce trap densities there also represent a promising approach to reduce the  $V_{OC}$  gap with the radiative limit. We note that there are examples in literature of boosting the  $V_{OC}$  by introduction of a porous HTL, compatible with high-temperatures, namely  $NiO_x$ .<sup>[69,75]</sup> Additionally, according to our numerical simulation the  $V_{OC}$  could be boosted by increasing the work-function of carbon-based contact or by reducing the surface recombination velocity of the minority carriers at the back-contact (Figure S16, Supporting Information). However, even if the band-alignment would be close to ideal in H-CPSCs, the  $V_{OC}$  would always be limited by the QFLS in perovskite, implying that the non-radiative losses of the photoabsorber itself or at its interfaces need to be reduced in order to obtain a  $V_{OC}$  beyond 1.1 V.

- ii. In the studied L-CPSCs, the largest losses were due to a non-ideal FF and  $J_{SC}$ . Based on the results from electrochemical impedance spectroscopy (EIS), only reducing the interfacial resistance at perovskite/carbon contact to the same value as it is in H-CPSCs would result in a 15% increase in FF, leading to the total FF value of >77%. We have recently demonstrated that the perovskite/carbon contact can be improved by alteration of the graphite powder type.<sup>[71]</sup> In addition, several reports have shown that the interfacial resistance can be strongly reduced by a press-transfer technique, which resulted in cell efficiencies above 17% (although the reported PV devices had a HTL).<sup>[76,77,78]</sup> Moreover, Liu et al. have shown how interfacial post-treatment with cesium acetate (CsAc) effectively reduces the interfacial resistance at the back-contact and suppresses non-radiative recombination.<sup>[79]</sup> In addition, increasing the work-function at the perovskite/carbon interface (Figure S13, Supporting Information) could further improve the performance of such cells.

Both cell types also suffer from optical losses, which in case of L-CPSCs could be alleviated for example by the use of indium-doped tin oxide (ITO) as a front electrode, which has less parasitic absorption. However, it was shown before that indium-doped tin oxide (ITO) tends to significantly increase its sheet resistivity when processed at high temperatures,<sup>[80]</sup> making it unfavorable for H-CPSCs. Naturally photon-management options (e.g., anti-reflective coating), inducing light-trapping is expected to boost the  $J_{SC}$  of the PSCs, regardless of the cell stack. Another promising strategy, which is possible in L-CPSCs, but not in H-CPSCs, is to integrate a reflective electron-blocking layer at the perovskite/contact, thereby allowing for transmitted photons in the long-wavelength region to be reflected back into the absorber (which often happens in conventional PSCs with metallic back-contact). Since in H-CPSCs the porous stack must be infiltrated with a perovskite solution only after all the porous layers are deposited, the integration of a compact reflective layer becomes problematic for solution infiltration. However, this problem does not occur in L-CPSCs, which are deposited layer by layer.

### 3. Conclusion

Although numerous works on PSCs with high- and low-temperature treated carbon electrodes have been demonstrated, their

quantitative comparison, comprehensive understanding of energy losses, and identification of promising improvement strategies were not shown up to now. In this work, for the first time we presented a detailed analysis of the fundamental losses in the two basic types of PSCs with carbon-based counter electrodes complemented by providing the necessary knowledge for further efforts on boosting their PCE. The presented study was aimed at resolving the fundamental differences between the H-CPSCs and L-CPSCs, with as few differences in cell stack as possible, in order to attribute the main differences in cell properties to the absorber itself or to its interface with the charge-transport layers. Therefore, the goal of our work was not to produce most efficient devices (as we did not utilize any hole-transport layer for a more objective comparison), but rather to understand where lie the efficiency gaps of both types of cells and what the most effective strategies to improve a device in both configurations could be.

PV devices with contacts treated at high-temperatures (H-CPSCs) contain perovskite crystals, which are constrained to <20 nm size due to process limitations, causing numerous grain-boundaries. As a result, the grain-boundaries cause excessive non-radiative recombination (even for the case of reduced trap densities), which brings down the charge carrier lifetime, PL intensity, and hence QFLS of the neat perovskite and complete cell stack, which consequently strongly limits the  $V_{OC}$  (<950 mV) of the manufactured solar cells. In addition, it causes a higher ideality factor and  $J_0$ , negatively affecting the FF. Although the PCE of such cells was higher than that of L-CPSCs due to higher  $J_{SC}$  and FF, it contains a great potential for further performance improvement if the issue of non-radiative recombination at the grain-boundaries can be solved. Even if the hole-selectivity at the back-contact would be further improved, the low QFLS of the perovskite crystals embedded in mesoporous layers of such cells would still limit the cell potential. Therefore, the most promising route to boost the efficiency of H-CPSCs in the future would be to alter the pore size to accommodate larger perovskite crystals and reduce non-radiative recombination at the grain-boundaries.

In devices where the carbon-based back-contacts are treated at low temperatures (L-CPSCs) and deposited afterwards on top of the perovskite, larger perovskite crystals can be formed. Despite the fact that the perovskite elementary composition was identical in both investigated architectures, we found that larger crystals of planar perovskite in L-CPSC strongly improve the carrier lifetime (from 72.9 ns to almost 1.8  $\mu$ s), enhance the QFLS to 1.192 eV (compared to 1.15 eV for H-CPSC), and allow for  $V_{OC}$  above 1.1 V in HTL-free cells. Although the PCE of L-CPSCs was lower due to worse charge carrier extraction and transport, high quality of the perovskite absorber provides a strong potential for improvements, especially considering that L-CPSCs offer a higher flexibility for cell stack alteration than H-CPSCs (due to high temperature processing of the latter). Adding HTLs with high hole mobilities and improving the contact between the back-electrode and the layers underneath is the key to unleashing the whole potential of the L-CPSCs.

The findings presented in this work are aimed to scrutinize the fundamental differences between these two types of CPSCs, demonstrating their losses and showing effective strategies to improve the PCE of such cells, in order to close the efficiency gap with the conventional PSCs with metal-based contacts.

## Supporting Information

Supporting Information is available from the Wiley Online Library or from the author.

## Acknowledgements

This work has been partially funded within the projects PROPER financed from the German Ministry of Education and Research under funding number 01DR19007 and UNIQUE supported under umbrella of SOLAR-ERA.NET\_cofund by ANR, Ptj, MIUR, MINECO-AEI, and SWEA, within the EU's HORIZON 2020 Research and Innovation Program (cofund ERA-NET Action No. 691664). D.B. acknowledges the scholarship support of the German Federal Environmental Foundation (DBU) and S.Z. acknowledges the scholarship support of the German Academic Exchange Service (DAAD). B.Y. and A.Ha. acknowledge the funding from the European Union's Horizon 2020 research and innovation program ESPRESSO under the agreement No.: 764047. This work has also been partially funded by Swiss National Science Foundation with Project No. 200020\_185041. T.D. acknowledges a National University of Ireland Travelling Studentship. K.F. acknowledges a George and Lilian Schiff Studentship, Winton Studentship, the Engineering and Physical Sciences Research Council (EPSRC) studentship, Cambridge Trust Scholarship, and Robert Gardiner Scholarship. S.D.S. acknowledges support from the Royal Society and Tata Group (UF150033). The work has received funding from the European Research Council under the European Union's Horizon 2020 research and innovation programme (HYPERION - grant agreement no. 756962). The authors acknowledge EPSRC (EP/R023980/1) for funding. M.A. acknowledges funding from the European Union's Horizon 2020 research and innovation program under the Marie Skłodowska-Curie grant agreement No. 841386, as well as from the Leverhulme Trust and the Isaac Newton Trust under an Early Career Fellowship (ECF-2019-224). The authors would like to thank Maryamsadat Heydarian and Laura Stevens for their EQE and AFM measurements.

## Conflicts of interest

D.Ma., S.N., and A.V. are employees of Solaronix SA, A.Ha. is a co-founder of Dyenamo AB, and S.D.S. is a co-founder of Swift Solar.

## Author Contributions

D.B. and L.W. have generated the concept of this publication, coordinated the work, analyzed all the measurements, and prepared the manuscript, as well as figures. B.Y. and J.S. have manufactured the samples for analyzing the properties of perovskite solar cells with low-temperature carbon-based contacts (L-CPSCs). D.Ma., S.N., and A.V. have manufactured the samples for analyzing the properties of perovskite solar cells with high-temperature carbon-based contacts (H-CPSCs). B.Y. has performed the TRPL and XRD measurements. D.B. has created a numerical model for simulation of CPSCs using SCAPS. M.A. and T.D. have performed the spatially resolved absolute hyperspectral PL measurement, from which the PL- and QFLS-maps were extracted by K.F., using a Python-based script. D.Mü. and D.B. have measured the light-intensity dependent behavior of the CPSCs'  $V_{OC}$  and  $J_{SC}$ . J.P.H. has performed and analyzed the LBIC-measurement. D.B. has measured the  $J-V$  characteristics of all the manufactured solar cells, spatially resolved PL, used for evaluating the charge-extraction from the solar cells and has also performed the EIS measurements together with S.Z., L.W., U.W., A.Hi., A.Ha., and S.D.S. have provided important conceptual ideas, contributed to the manuscript preparation and results interpretation. All authors have made valuable comments to the manuscript.

Open Access funding enabled and organized by Projekt DEAL.

## Data Availability Statement

The data that support the findings of this study are available in the supplementary material of this article.

## Keywords

carbon-based electrodes, HTL-free, perovskites, photovoltaics, recombination

Received: October 8, 2021

Revised: December 2, 2021

Published online:

- [1] Y. Rong, Y. Hu, A. Mei, H. Tan, M. I. Saidaminov, S. I. Seok, M. D. McGehee, E. H. Sargent, H. Han, *Science* **2018**, *361*, eaat8235.
- [2] J. Y. Kim, J.-W. Lee, H. S. Jung, H. Shin, N.-G. Park, *Chem. Rev.* **2020**, *120*, 7867.
- [3] J.-P. Correa-Baena, M. Saliba, T. Buonassisi, M. Grätzel, A. Abate, W. Tress, A. Hagfeldt, *Science* **2017**, *358*, 739.
- [4] Q. Wang, N. Phung, D. Di Girolamo, P. Vivo, A. Abate, *Energy Environ. Sci.* **2019**, *12*, 865.
- [5] B. Chen, P. N. Rudd, S. Yang, Y. Yuan, J. Huang, *Chem. Soc. Rev.* **2019**, *48*, 3842.
- [6] L. Fu, H. Li, L. Wang, R. Yin, B. Li, L. Yin, *Energy Environ. Sci.* **2020**, *13*, 4017.
- [7] S. Liu, Y. Guan, Y. Sheng, Y. Hu, Y. Rong, A. Mei, H. Han, *Adv. Energy Mater.* **2020**, *10*, 1902492.
- [8] T. Li, Y. Pan, Z. Wang, Y. Xia, Y. Chen, W. Huang, *J. Mater. Chem. A* **2017**, *5*, 12602.
- [9] C. C. Boyd, R. Checharoen, K. A. Bush, R. Prasanna, T. Leijtens, M. D. McGehee, *ACS Energy Lett.* **2018**, *3*, 1772.
- [10] S. Wu, R. Chen, S. Zhang, B. H. Babu, Y. Yue, H. Zhu, Z. Yang, C. Chen, W. Chen, Y. Huang, S. Fang, T. Liu, L. Han, W. Chen, *Nat. Commun.* **2019**, *10*, 1161.
- [11] D. Bogachuk, K. Sadeddine, D. Martineau, S. Narbey, A. Verma, P. Gebhardt, J. P. Herterich, N. Glissmann, S. Zouhair, J. Markert, I. E. Gould, M. D. McGehee, U. Würfel, A. Hinsch, L. Wagner, *Sol. RRL* **2022**, 2100527.
- [12] G. Grancini, C. Roldán-Carmona, I. Zimmermann, E. Mosconi, X. Lee, D. Martineau, S. Narbey, F. Oswald, F. de Angelis, M. Graetzel, M. K. Nazeeruddin, *Nat. Commun.* **2017**, *8*, 15684.
- [13] A. Mei, Y. Sheng, Y. Ming, Y. Hu, Y. Rong, W. Zhang, S. Luo, G. Na, C. Tian, X. Hou, Y. Xiong, Z. Zhang, S. Liu, S. Uchida, T.-W. Kim, Y. Yuan, L. Zhang, Y. Zhou, H. Han, *Joule* **2020**, *4*, 2646.
- [14] D. Bogachuk, S. Zouhair, K. Wojciechowski, B. Yang, V. Babu, L. Wagner, B. Xu, J. Lim, S. Mastroianni, H. Pettersson, A. Hagfeldt, A. Hinsch, *Energy Environ. Sci.* **2020**, *13*, 3880.
- [15] Z. Ku, Y. Rong, M. Xu, T. Liu, H. Han, *Sci. Rep.* **2013**, *3*, 3132.
- [16] Z. Song, S. C. Watthage, A. B. Phillips, B. L. Tompkins, R. J. Ellingson, M. J. Heben, *Chem. Mater.* **2015**, *27*, 4612.
- [17] L. Wagner, S. Mastroianni, A. Hinsch, *Joule* **2020**, *4*, 882.
- [18] F. Meng, A. Liu, L. Gao, J. Cao, Y. Yan, N. Wang, M. Fan, G. Wei, T. Ma, *J. Mater. Chem. A* **2019**, *7*, 8690.
- [19] Y. Hu, S. Si, A. Mei, Y. Rong, H. Liu, X. Li, H. Han, *Sol. RRL* **2017**, *1*, 1600019.
- [20] F. Zhang, X. Yang, H. Wang, M. Cheng, J. Zhao, L. Sun, *ACS Appl. Mater. Interfaces* **2014**, *6*, 16140.
- [21] H. Zhou, Y. Shi, Q. Dong, H. Zhang, Y. Xing, K. Wang, Y. Du, T. Ma, *J. Phys. Chem. Lett.* **2014**, *5*, 3241.
- [22] K. Ramachandran, C. Jegannathan, S. Karuppachamy, *J. Alloys Compd.* **2021**, *881*, 160530.

- [23] X. Xiao, Y. Chu, C. Zhang, Z. Zhang, Z. Qiu, C. Qiu, H. Wang, A. Mei, Y. Rong, G. Xu, Y. Hu, H. Han, *Fundam. Res.* **2021**, *1*, 385.
- [24] K. R. Taretto, *Modeling and Characterization of Polycrystalline Silicon for Solar Cells and Microelectronics*, University of Stuttgart, xxxx **2003**.
- [25] K.-D. Jäger, O. Isabella, A. H. M. Smets, R. A. van Swaaij, M. Zeman, *Solar Energy: Fundamentals, Technology and Systems*, UIT, Cambridge **2016**.
- [26] T. S. Sherkar, C. Momblona, L. Gil-Escrig, J. Ávila, M. Sessolo, H. J. Bolink, L. J. A. Koster, *ACS Energy Lett.* **2017**, *2*, 1214.
- [27] A.-F. Castro-Méndez, J. Hidalgo, J.-P. Correa-Baena, *Adv. Energy Mater.* **2019**, *9*, 1901489.
- [28] J. S. Yun, J. Seidel, J. Kim, A. M. Soufiani, S. Huang, J. Lau, N. J. Jeon, S. I. Seok, M. A. Green, A. Ho-Baillie, *Adv. Energy Mater.* **2016**, *6*, 1600330.
- [29] D. W. de Quilletes, S. M. Vorpahl, S. D. Stranks, H. Nagaoka, G. E. Eperon, M. E. Ziffer, H. J. Snaith, D. S. Ginger, *Science* **2015**, *348*, 683.
- [30] E. M. Tennyson, T. A. S. Doherty, S. D. Stranks, *Nat. Rev. Mater.* **2019**, *4*, 573.
- [31] G. Landi, H. C. Neitzert, C. Barone, C. Mauro, F. Lang, S. Albrecht, B. Rech, S. Pagano, *Adv. Sci. (Weinh)* **2017**, *4*, 1700183.
- [32] J. S. Yun, A. Ho-Baillie, S. Huang, S. H. Woo, Y. Heo, J. Seidel, F. Huang, Y.-B. Cheng, M. A. Green, *J. Phys. Chem. Lett.* **2015**, *6*, 875.
- [33] W. Tress, N. Marinova, O. Inganäs, M. K. Nazeeruddin, S. M. Zakeeruddin, M. Graetzel, *Adv. Energy Mater.* **2015**, *5*, 1400812.
- [34] W. Tress, *Adv. Energy Mater.* **2017**, *7*, 1602358.
- [35] K. Tvingstedt, O. Malinkiewicz, A. Baumann, C. Deibel, H. J. Snaith, V. Dyakonov, H. J. Bolink, *Sci. Rep.* **2014**, *4*, 6071.
- [36] J. M. Ball, A. Petrozza, *Nat. Energy* **2016**, *1*, 16149.
- [37] S. D. Stranks, H. J. Snaith, *Nat. Nanotechnol.* **2015**, *10*, 391.
- [38] S. D. Stranks, V. M. Burlakov, T. Leijtens, J. M. Ball, A. Goriely, H. J. Snaith, *Phys. Rev. Appl.* **2014**, *2*, 034007.
- [39] T. Liu, Y. Rong, Y. Xiong, A. Mei, Y. Hu, Y. Sheng, P. Jiang, X. Hou, M. Duan, Y. Guan, L. Hong, H. Han, *RSC Adv.* **2017**, *7*, 10118.
- [40] M. Stolterfoht, M. Grischek, P. Caprioglio, C. M. Wolff, E. Gutierrez-Partida, F. Peña-Camargo, D. Rothhardt, S. Zhang, M. Raoufi, J. Wolansky, M. Abdi-Jalebi, S. D. Stranks, S. Albrecht, T. Kirchartz, D. Neher, *Adv. Mater.* **2020**, *32*, 2000080.
- [41] L. Krückemeier, U. Rau, M. Stolterfoht, T. Kirchartz, *Adv. Energy Mater.* **2020**, *10*, 1902573.
- [42] A. Mei, X. Li, L. Liu, Z. Ku, T. Liu, Y. Rong, M. Xu, M. Hu, J. Chen, Y. Yang, M. Grätzel, H. Han, *Science* **2014**, *345*, 295.
- [43] T. Liu, L. Liu, M. Hu, Y. Yang, L. Zhang, A. Mei, H. Han, *J. Power Sources* **2015**, *293*, 533.
- [44] G. Grancini, C. Roldán-Carmona, I. Zimmermann, E. Mosconi, X. Lee, D. Martineau, S. Narbey, F. Oswald, F. De Angelis, M. Graetzel, M. K. Nazeeruddin, *Nat. Commun.* **2017**, *8*, 15684.
- [45] H. Lakhiani, T. Dunlop, F. de Rossi, S. Dimitrov, R. Kerremans, C. Charbonneau, T. Watson, J. Barbé, W. C. Tsoi, *Adv. Funct. Mater.* **2019**, *29*, 1900885.
- [46] Y. Zhou, N. P. Padture, in *2020 47th IEEE Photovoltaic Spec. Conf. (PVSC)*, **2020**, p. 2316.
- [47] S. Wieghold, J.-P. Correa-Baena, L. Nienhaus, S. Sun, K. E. Shulenberger, Z. Liu, J. S. Tresback, S. S. Shin, M. G. Bawendi, T. Buonassisi, *ACS Appl. Energy Mater.* **2018**, *1*, 6801.
- [48] X. Ren, Z. Yang, D. Yang, X. Zhang, D. Cui, Y. Liu, Q. Wei, H. Fan, S. F. Liu, *Nanoscale* **2016**, *8*, 3816.
- [49] H. Fan, F. Li, P. Wang, Z. Gu, J.-H. Huang, K.-J. Jiang, B. Guan, L.-M. Yang, X. Zhou, Y. Song, *Nat. Commun.* **2020**, *11*, 5402.
- [50] S. Jariwala, H. Sun, G. W. P. Adhyaksa, A. Lof, L. A. Muscarella, B. Ehrler, E. C. Garnett, D. S. Ginger, *Joule* **2019**, *3*, 3048.
- [51] I. Mela, C. Poudel, M. Anaya, G. Delpont, K. Frohna, S. Macpherson, T. A. S. Doherty, A. Scheeder, S. D. Stranks, C. F. Kaminski, *Adv. Funct. Mater.* **2021**, *31*, 2100293.
- [52] G. W. P. Adhyaksa, S. Brittman, H. Āboliņš, A. Lof, X. Li, J. D. Keelor, Y. Luo, T. Duevski, R. M. A. Heeren, S. R. Ellis, D. P. Fenning, E. C. Garnett, *Adv. Mater.* **2018**, *30*, 1804792.
- [53] H. Sun, G. W. Adhyaksa, E. C. Garnett, *Adv. Energy Mater.* **2020**, *10*, 2000364.
- [54] S. Mastroianni, F. D. Heinz, J.-H. Im, W. Veurman, M. Padilla, M. C. Schubert, U. Würfel, M. Grätzel, N.-G. Park, A. Hinsch, *Nanoscale* **2015**, *7*, 19653.
- [55] Z. Zhang, M. Wang, L. Ren, K. Jin, *Sci. Rep.* **2017**, *7*, 1918.
- [56] V. D'Innocenzo, A. R. Srimath Kandada, M. de Bastiani, M. Gandini, A. Petrozza, *J. Am. Chem. Soc.* **2014**, *136*, 17730.
- [57] G. Grancini, S. Marras, M. Prato, C. Giannini, C. Quarti, F. de Angelis, M. de Bastiani, G. E. Eperon, H. J. Snaith, L. Manna, A. Petrozza, *J. Phys. Chem. Lett.* **2014**, *5*, 3836.
- [58] L. Wagner, L. E. Mundt, G. Mathiazhagan, M. Mundus, M. C. Schubert, S. Mastroianni, U. Würfel, A. Hinsch, S. W. Glunz, *Sci. Rep.* **2017**, *7*, 14899.
- [59] G. El-Hajje, C. Momblona, L. Gil-Escrig, J. Ávila, T. Guillemot, J.-F. Guillemoles, M. Sessolo, H. J. Bolink, L. Lombez, *Energy Environ. Sci.* **2016**, *9*, 2286.
- [60] K. Frohna, M. Anaya, S. Macpherson, J. Sung, T. A. S. Doherty, Y.-H. Chiang, A. J. Winchester, K. W. P. Orr, J. E. Parker, P. D. Quinn, K. M. Dani, A. Rao, S. D. Stranks, *Nat. Nanotechnol.* **2021**.
- [61] M. Stolterfoht, C. M. Wolff, J. A. Márquez, S. Zhang, C. J. Hages, D. Rothhardt, S. Albrecht, P. L. Burn, P. Meredith, T. Unold, D. Neher, *Nat. Energy* **2018**, *3*, 847.
- [62] D. Abou-Ras, T. Kirchartz, U. Rau, *Advanced Characterization Techniques for Thin Film Solar Cells*, Wiley Online Library, New York **2011**.
- [63] M. Stolterfoht, P. Caprioglio, C. M. Wolff, J. A. Márquez, J. Nordmann, S. Zhang, D. Rothhardt, U. Hörmann, Y. Amir, A. Redinger, L. Kegelmann, F. Zu, S. Albrecht, N. Koch, T. Kirchartz, M. Saliba, T. Unold, D. Neher, *Energy Environ. Sci.* **2019**, *12*, 2778.
- [64] J. J. Choi, X. Yang, Z. M. Norman, S. J. L. Billinge, J. S. Owen, *Nano Lett.* **2014**, *14*, 127.
- [65] B. Yang, J. Suo, F. Di Giacomo, S. Olthof, D. Bogachuk, Y. Kim, X. Sun, L. Wagner, F. Fu, S. M. Zakeeruddin, A. Hinsch, M. Grätzel, A. Di Carlo, A. Hagfeldt, *ACS Energy Lett.* **2021**, *6*, 3916.
- [66] L. Zhou, Y. Zuo, T. K. Mallick, S. Sundaram, *Sci. Rep.* **2019**, *9*, 8778.
- [67] Jiangzhao Chen, Yuli Xiong, Yaoguang Rong, Anyi Mei, Yusong Sheng, Pei Jiang, Yue Hu, Xiong Li, Hongwei Han, *Nano Energy* **2016**, *27*, 130.
- [68] Q.-Q. Chu, B. Ding, Q. Qiu, Y. Liu, C.-X. Li, C.-J. Li, G.-J. Yang, B. Fang, *J. Mater. Chem. A* **2018**, *6*, 8271.
- [69] X. Xu, Z. Liu, Z. Zuo, M. Zhang, Z. Zhao, Y. Shen, H. Zhou, Q. Chen, Y. Yang, M. Wang, *Nano Lett.* **2015**, *15*, 2402.
- [70] L. Wagner, P. Schygulla, J. P. Herterich, M. Elshamy, D. Bogachuk, S. Zouhair, S. Mastroianni, U. Würfel, Y. Liu, S. M. Zakeeruddin, M. Grätzel, arXiv preprint arXiv:2110.09353, **2021**.
- [71] D. Bogachuk, R. Tsuji, D. Martineau, S. Narbey, J. P. Herterich, L. Wagner, K. Suginuma, S. Ito, A. Hinsch, *Carbon* **2021**, *178*, 10.
- [72] L. Wagner, S. Chacko, G. Mathiazhagan, S. Mastroianni, A. Hinsch, *ACS Energy Lett.* **2018**, *3*, 1122.
- [73] J. Shao, S. Yang, L. Lei, Q. Cao, Y. Yu, Y. Liu, *Chem. Mater.* **2016**, *28*, 7134.
- [74] Y. Tanaka, S. L. Lim, W. P. Goh, C. Jiang, S. Y. Tee, T. Ye, X. Li, K. H. Nguyen, C. J. J. Lee, N. Ding, Z. Liu, J. Wu, J. Zhang, M.-Y. Han, *ChemNanoMat* **2018**, *4*, 394.
- [75] S. Liu, W. Huang, P. Liao, N. Pootrakulchote, H. Li, J. Lu, J. Li, F. Huang, X. Shai, X. Zhao, Y. Shen, Y.-B. Cheng, M. Wang, *J. Mater. Chem. A* **2017**, *5*, 22952.
- [76] H. Zhang, J. Xiao, J. Shi, H. Su, Y. Luo, D. Li, H. Wu, Y.-B. Cheng, Q. Meng, *Adv. Funct. Mater.* **2018**, *28*, 1802985.

- [77] H. Su, J. Xiao, Q. Li, C. Peng, X. Zhang, C. Mao, Q. Yao, Y. Lu, Z. Ku, J. Zhong, W. Li, Y. Peng, F. Huang, Y.-B. Cheng, *Mater. Sci. Semicond. Process.* **2020**, *107*, 104809.
- [78] Y. Yang, M. T. Hoang, D. Yao, N. D. Pham, V. T. Tiong, X. Wang, H. Wang, *J. Mater. Chem. A* **2020**, *8*, 12723.
- [79] T. Liu, Z. Wang, L. Lou, S. Xiao, S. Zheng, S. Yang, *Sol. RRL* **2020**, *4*, 1900278.
- [80] M. Zhang, B. Wilkinson, Y. Liao, J. Zheng, C. F. J. Lau, J. Kim, J. Bing, M. A. Green, S. Huang, A. W.-Y. Ho-Baillie, *Joule* **2018**, *2*, 2694.